Available online at www.sciencedirect.com
SCIENCE DIRECT®
Journal of Computational Physics 212 (2006) 268–287
JOURNAL OF COMPUTATIONAL PHYSICS
www.elsevier.com/locate/jcp

On the streamfunction–vorticity formulation in sliding bi-period frames: Application to bulk behavior for polymer blends

Patrick D. Anderson *, Bert J. Keestra, Martien A. Hulsen

Materials Technology, Dutch Polymer Institute, Eindhoven University of Technology, P.O. Box 513, 5600 MB Eindhoven, The Netherlands

Received 11 October 2004; received in revised form 30 May 2005; accepted 4 July 2005
Available online 18 August 2005

Abstract

The Lees–Edwards description of bi-periodic boundary conditions has been extended to the streamfunction and streamfunction–vorticity formulation in sliding bi-periodic frames. The required compatibility conditions are formulated and uniqueness of the solution is shown. The model has been implemented in a spectral element method context to describe bulk shear behavior far away from walls, where no simple periodic boundary conditions can be used. In the numerical model a Lagrangian multiplier is introduced to couple the shearing boundaries. The proposed method has been validated for a mathematical test problem; convergence is shown and the influence of the order of approximation of the Lagrangian multiplier is studied. Finally, results are presented for drop coalescence across the boundaries of the bi-periodic frame.

Keywords: Lees–Edwards boundary conditions; Streamfunction–vorticity formulation; Lagrangian multiplier; Polymer blends

1. Introduction

Blending or mixing of immiscible polymers offers an attractive and efficient route to produce 'new' materials with tailor made properties. The mechanical properties of these multi-phase polymer blends are intimately connected with the morphology imparted during processing. Hence, understanding the connection between applied flow and morphology development is vital to optimize the processing and therefore the

* Corresponding author. Tel.: +31402474823; fax: +31402447355.
E-mail address: p.d.anderson@tue.nl (P.D. Anderson).

0021-9991/$ - see front matter © 2005 Elsevier Inc. All rights reserved.
doi:10.1016/j.jcp.2005.07.002

resulting properties of blends. In the literature a large number of comprehensive experimental and theoretical studies of the morphology development in simple (shear) flow fields are reported, and some of this work is summarized in the review by Tucker and Moldenaers [1]. Although considerable fundamental understanding of morphology changes during (shear) flow has been obtained already, the prediction of the (transient) rheology coupled with the micro structure development still remains a challenge. One of the main difficulties, which is addressed in the current paper, is the correct description of bulk shear behavior far away from the shearing walls.

In 1972, Lees and Edwards [2] proposed a bi-periodic domain concept for molecular dynamics simulations by describing sliding boundary conditions for simple shear flow, which is nowadays referred to as Lees–Edwards boundary conditions. Recently, this scheme has been used with the Lattice Boltzmann method to solve particle suspension [3] and phase separation problems [4,5]. It has also been applied to concentrated emulsion problems by a Lagrangian–Eulerian method with a re-meshing technique using Voronoi tessellation [6]. Hwang et al. [7] extended the sliding bi-periodic frame concept of Lees and Edwards for discrete particles to continuous fields and combined it with the velocity pressure formulation of the fictitious-domain/finite element method.

In this study the sliding-periodic frame is used to describe drop deformation, breakup and coalescence in a shear flow. Essentially, after formulating the corresponding flow equations for a blend of two Newtonian fluids in the absence of inertia, this reduces to the description of the streamfunction–vorticity formulation for Lees–Edwards boundary conditions which is the main objective of this paper. In general for the streamfunction–vorticity formulation with Dirichlet-type of boundary conditions complicated integral type boundary conditions need to be specified in order to obtain an equivalent formulation [8].

The manuscript is organized as follows: first a description is given of the sliding-periodic frame concept and the governing equations in both a streamfunction and a streamfunction–vorticity formulation are derived. In Section 4, the weak formulation of the latter is described and equivalence of the variational problem with the original strong form is shown. Details of the implementation are given where a Lagrangian multiplier is used to couple the shearing boundaries. In Section 5 the model is validated using a mathematical test example and *hp*-convergence is shown. Finally, the streamfunction–vorticity formulation is combined with the Cahn–Hilliard theory and the process of coalescence of drops across bi-period frames is studied.

2. Sliding frames

In order to describe bulk shear behavior far away from walls, the sliding frame concept of Lees and Edwards [2] can be used. This concept is illustrated in Fig. 1. If we have a steady shear flow characterized

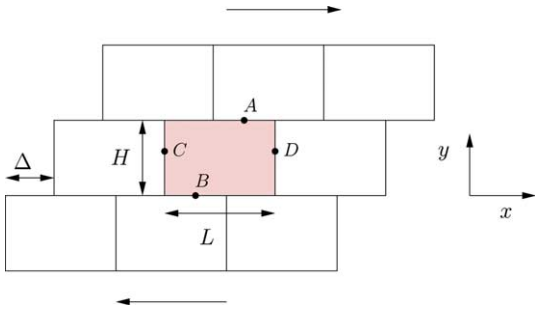

Fig. 1. Sliding frame concept of Lees–Edwards.

by an average shear rate $\dot{\gamma}$, each row of frames moves with a velocity such that the average linear velocity profile, relative to the frame, is the same in each frame. This means that the relative velocity between rows is $\dot{\gamma}H$ and that the amount of slide Δ between rows, see Fig. 1, is given by

$$\Delta = \dot{\gamma}Ht, \tag{1}$$

where H is the height of the frame and t is the time. Within each frame the linear velocity profile is given by

$$u = u_0 + \dot{\gamma}y, \quad v = 0, \tag{2}$$

where u and v are the velocity components in x and y direction, respectively, and y is the local coordinate within a frame ($y = 0$ at the lower boundary of a frame). When crossing a row boundary there is a jump in velocity of $-\dot{\gamma}H$ ($y = H$ in the first frame and $y = 0$ in the next). However, this is compensated by the frame velocity, which is $\dot{\gamma}H$ higher leading to a continuous velocity in a global stationary frame.

Now we assume that the velocity *relative within each frame* is the same and therefore the velocity be written as

$$u = \hat{u} + u_0 + \dot{\gamma}y, \quad v = \hat{v}, \tag{3}$$

where the perturbations from the linear profile $\hat{u}$ and $\hat{v}$ are continuous functions from *frame to frame* and are furthermore as smooth as needed for the theory, i.e. we can take derivatives as much as we need. Note, that due to the continuity of $\hat{u}$ and $\hat{v}$ the velocity in a stationary global frame is continuous when crossing frame boundaries. This is the essential feature of the sliding frame concept that cannot be achieved by taking periodical boundary conditions alone. The continuity of the velocity is particularly important when studying heterogeneous systems such as particles in flow or drop coalescence, such as studied is this paper.

Since the solution in each frame is identical we can restrict our efforts to a single frame only and transform the continuity requirements of $\hat{u}(x, y, t)$ and $\hat{v}(x, y, t)$ to boundary conditions in a single frame. In Fig. 2 we have depicted a single frame of width L and height H, where the points A and B (and C and D) within the full frame stacking of Fig. 1 are really the same points. This means that for the continuity requirements of $\hat{u}$ and $\hat{v}$ we can equivalently require the values in A and B (and C and D) within a frame to be the same or:

$$\text{Horizontal} : \hat{u}(0, y, t) = \hat{u}(L, y, t) \quad \text{for } y \in [0, H], \tag{4}$$

$$\text{Vertical} : \hat{u}(x, H, t) = \hat{u}(\{x - \dot{\gamma}Ht\}^{\star}, 0, t) \quad \text{for } x \in [0, L), \tag{5}$$

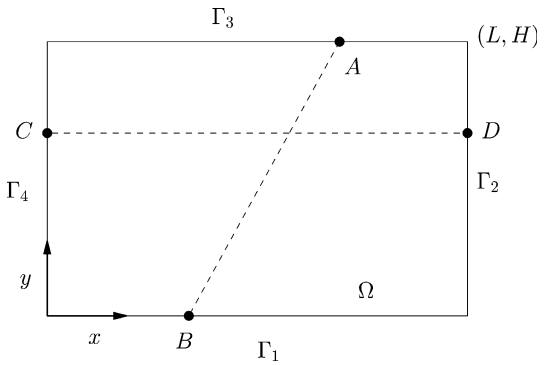

Fig. 2. A single frame. The domain is denoted by Ω. The boundary of the frame is $\Gamma = \bigcup_{i=1}^{4} \Gamma_i$.

and the same for $\hat{v}$. In Eq. (5), we have introduced the operator $\{\}^\star$ to denote the modulo L function [7]. In the following, we will call a function that fulfills Eqs. (4) and (5) to be *continuous sheared periodic*. For u and v this translates to the following periodic boundary conditions:

$$\text{Horizontal}: \begin{cases} u(0,y,t) = u(L,y,t) \\ v(0,y,t) = v(L,y,t) \end{cases} \quad \text{for } y \in [0,H], \tag{6}$$

$$\text{Vertical}: \begin{cases} u(x,H,t) = u(\{x - \dot{\gamma}Ht\}^\star, 0, t) + \dot{\gamma}H \\ v(x,H,t) = v(\{x - \dot{\gamma}Ht\}^\star, 0, t) \end{cases} \quad \text{for } x \in [0,L), \tag{7}$$

or u and v is *sheared periodic*, but only v is *continuous* and u is not.

3. Governing equations

3.1. Velocity–pressure formulation

We assume that the flow is governed by the Stokes problem

$$-\nabla p + \eta \nabla^2 \boldsymbol{u} = \boldsymbol{f} \quad \text{in } \Omega, \tag{8}$$

$$\nabla \cdot \boldsymbol{u} = 0 \text{ in } \Omega, \tag{9}$$

where $\boldsymbol{u} = (u, v)$ is the velocity vector, p is the pressure and η is the viscosity of the fluid. When studying the Stokes problem in a sliding frame we need, in addition to Eqs. (6) and (7), similar periodicity conditions for the traction on the boundary Γ, a pressure level and a level for the velocity components in both directions [7].

3.2. Streamfunction formulation

In order to eliminate the pressure and the incompressibility condition Eq. (9) we introduce the streamfunction ψ as follows:

$$u = \frac{\partial \psi}{\partial y}, \quad v = -\frac{\partial \psi}{\partial x}. \tag{10}$$

In this way, Eq. (9) is automatically satisfied. After applying the curl operator on Eq. (8) and substituting Eq. (10) we get the following biharmonic equation:

$$\nabla^4 \psi = g \text{ in } \Omega, \tag{11}$$

where

$$g = -\frac{1}{\eta}(\nabla \times \boldsymbol{f})_z = -\frac{1}{\eta}\left(\frac{\partial f_y}{\partial x} - \frac{\partial f_x}{\partial y}\right). \tag{12}$$

Using Eq. (3) and the definition of the streamfunction equation (10) we can split ψ as follows:

$$\psi = \hat{\psi} + u_0 y + \frac{1}{2}\dot{\gamma} y^2 \text{ in } \Omega, \tag{13}$$

where

$$\frac{\partial \hat{\psi}}{\partial x} = -\hat{v}, \quad \frac{\partial \hat{\psi}}{\partial y} = \hat{u}. \tag{14}$$

Without loss of generality we can safely assume that $\hat{\psi}$ is a continuous sheared periodic function or

$$\hat{\psi}(0,y,t) = \hat{\psi}(L,y,t) \quad \text{for } y \in [0,H], \tag{15}$$

$$\hat{\psi}(x,H,t) = \hat{\psi}(\{x-\dot{\gamma}Ht\}^{\star},0,t) \quad \text{for } x \in [0,L). \tag{16}$$

The reason is that because of the sheared periodicity of $\hat{u}$ and $\hat{v}$ together with Eq. (14) the "profile" of $\hat{\psi}$ is the same along the boundaries Γ_1 and Γ_3 (and Γ_2 and Γ_4), except that they differ by a constant. The constant between Γ_1 and Γ_3 is the "flux" through any curve connecting A and B in Fig. 2 (for Γ_2 and Γ_4 it is the flux through any curve connecting C and D). By adjusting the frame velocity in x and y direction we can always make the fluxes equal to zero. Adjusting the frame velocity is allowed because the absolute velocity of the frame has no physical significance when inertia has been neglected. This is related to the necessary specification of the level of the velocity in the velocity–pressure formulation of the sliding periodic frame [7].

Again for the same reason that translational velocities are of no physical importance here, we can safely take $u_0 = -\frac{1}{2}\dot{\gamma}H$, leading to

$$\psi = \hat{\psi} - \frac{1}{2}\dot{\gamma}(yH - y^2), \tag{17}$$

which means that ψ is continuous sheared periodic and $\partial\psi/\partial y$ follows the boundary conditions for u:

$$\frac{\partial\psi}{\partial y}(0,y,t) = \frac{\partial\psi}{\partial y}(L,y,t) \quad \text{for } y \in [0,H], \tag{18}$$

$$\frac{\partial\psi}{\partial y}(x,H,t) = \frac{\partial\psi}{\partial y}(\{x-\dot{\gamma}Ht\}^{\star},0,t) + \dot{\gamma}H \quad \text{for } x \in [0,L), \tag{19}$$

where we have used that $\hat{u} = \partial\hat{\psi}/\partial y$ is continuous sheared periodic. Note, that all other derivatives and higher-order derivatives are continuous sheared periodic, when needed for the theory.

In the next section, when dealing with the weak forms, we will show that ψ can be determined uniquely up to an integration constant, provided we fulfill the compatibility condition

$$\int_{\Omega} g \, \mathrm{d}\Omega = 0. \tag{20}$$

Using Eq. (12) and Stokes' theorem we find that

$$\int_{\Omega} g \, \mathrm{d}\Omega = -\frac{1}{\eta}\int_{\Gamma} \boldsymbol{t}\cdot\boldsymbol{f} \; \mathrm{d}\Gamma = 0, \tag{21}$$

where $\boldsymbol{t}$ is the unit vector tangential to the boundary Γ. We have used that $\boldsymbol{f}$ is a sheared periodic function. In our two-phase system, see Section 5.2, we have $\boldsymbol{f} = -\rho\mu\nabla c$ and therefore fulfills this condition.

3.3. Streamfunction–vorticity formulation

The streamfunction formulation leads to a biharmonic equation (11) which, within a variational context, leads to severe continuity requirements. Therefore Eq. (11) is usually split into two Poisson equations in the following way:

$$-\nabla^2\omega = g \text{ in } \Omega, \tag{22}$$

$$-\nabla^2\psi = \omega \text{ in } \Omega, \tag{23}$$

where we have introduced the vorticity ω as

$$\omega = \frac{\partial v}{\partial x} - \frac{\partial u}{\partial y}. \tag{24}$$

In the next section, where we will describe the weak forms, we will show that we need to fulfill the compatibility conditions

$$\int_\Omega g \, \mathrm{d}\Omega = 0, \tag{25}$$

$$\int_\Omega \omega \, \mathrm{d}\Omega = -\dot{\gamma} LH, \tag{26}$$

in order to be consistent with the streamfunction formulation. Eq. (25) is the same as the compatibility condition in the streamfunction formulation and is fulfilled. The streamfunction ψ can again be determined uniquely up to an integration constant and the vorticity is a unique function. Eq. (26), which is a constraint on ω for Eq. (22), can be implemented using a Lagrangian multiplier. However, it is easier to solve Eq. (22) with a prescribed (Dirichlet) value in a single point (say $\tilde{\omega}$ is the solution). Then add an arbitrary constant c

$$\omega = \tilde{\omega} + c. \tag{27}$$

Applying Eq. (26) leads to

$$c = -\dot{\gamma} - \frac{1}{LH} \int_\Omega \tilde{\omega} \, \mathrm{d}\Omega. \tag{28}$$

Notice, that Eqs. (22) and (26) are fully decoupled from Eq. (23) if g does not depend on ψ.

4. Weak formulation

We will now derive the weak formulation of Eqs. (22) and (23) for use in the spectral element discretization and for a proof of the uniqueness. After multiplying Eqs. (22) and (23) by test functions w_1 and w_2, respectively, integrating over the domain Ω and partial integration of the second-order terms we get

$$(\nabla\omega, \nabla w_1) - \left(\frac{\partial\omega}{\partial n}, w_1\right)_\Gamma = (g, w_1) \quad \text{for all } w_1, \tag{29}$$

$$(\nabla\psi, \nabla w_2) - \left(\frac{\partial\psi}{\partial n}, w_2\right)_\Gamma = (\omega, w_2) \quad \text{for all } w_2, \tag{30}$$

where we have defined

$$(a,b) = \int_\Omega ab \, \mathrm{d}\Omega, (a,b)_\Gamma = \int_\Gamma ab \, \mathrm{d}\Gamma. \tag{31}$$

We now assume that w_1 and w_2 are continuous sheared periodic test functions. Furthermore, we assume that ω and ψ are also continuous sheared periodic functions, that $\partial\omega/\partial n$ fulfills

$$\begin{aligned} &\frac{\partial\omega}{\partial n}(0,y,t) = -\frac{\partial\omega}{\partial n}(L,y,t) \quad \text{for } y \in [0,H], \\ &\frac{\partial\omega}{\partial n}(x,H,t) = -\frac{\partial\omega}{\partial n}(\{x - \dot{\gamma}Ht\}^\star, 0, t) \quad \text{for } x \in [0,L), \end{aligned} \tag{32}$$

and that $\partial\psi/\partial n$ obeys

$$\begin{aligned}\frac{\partial\psi}{\partial n}(0,y,t) &= -\frac{\partial\psi}{\partial n}(L,y,t) \quad \text{for } y \in [0,H],\\ \frac{\partial\psi}{\partial n}(x,H,t) &= -\frac{\partial\psi}{\partial n}(\{x-\dot{\gamma}Ht\}^{\star},0,t) + \dot{\gamma}H \quad \text{for } x \in [0,L).\end{aligned} \tag{33}$$

Note that $\boldsymbol{n}$ is the outside normal and that the boundary conditions are fully consistent with the previous section. Using these boundary conditions we get the following weak formulation: Find continuous sheared periodic functions ω and ψ such that

$$(\nabla\omega, \nabla w_1) = (g, w_1), \tag{34}$$

$$(\nabla\psi, \nabla w_2) - (\dot{\gamma}H, w_2)_{\Gamma_3} = (\omega, w_2), \tag{35}$$

for all continuous sheared periodic test functions w_1 and w_2. Reversely, it is easy to show that if the weak form is fulfilled, the original equations (22) and (23) and the boundary conditions equations (32) and (33) are retained. Hence, the variational problem is fully equivalent to the original strong form.

Hiding in Eqs. (34) and (35) are two compatibility conditions, similar to the compatibility relation between the source terms and the normal fluxes through the boundary for a Poisson equation with full Neumann boundary conditions. Substituting $w_1 = 1$ and $w_2 = 1$ into Eqs. (34) and (35) we get Eqs. (25) and (26), respectively. These compatibility conditions must be fulfilled beforehand, because the variables being solved, ω and ψ, respectively, are not present in these equations. The uniqueness of the ψ and ω are proven in Appendix A.

4.1. Implementation

The implementation of the streamfunction formulation in a sliding bi-periodic domain is complicated by the fact that nodal points on the top and bottom boundary of the domain are not coupled with the same x-coordinate, but shifted with an amount that depends on the shear-rate $\dot{\gamma}$, elapsed time t and height H of the domain. A Lagrangian multiplier λ is used to couple the unknown, say a for either ω or ψ (or c or μ, see Section 5.2), on the top and bottom boundary in the following way:

$$\int_{\partial\Omega^{\text{up}}} \lambda(x)[a(x,H,t) - a(\{x-\dot{\gamma}Ht\}^{*},0,t)]\,\mathrm{d}\Gamma = 0. \tag{36}$$

For reasons explained in the following and illustrated in Fig. 3, the integral in equation (36) is split into two parts and evaluated per element:

$$\int_{\partial\Omega_e^{\text{up}}} \lambda(x)a(x,H,t)\,\mathrm{d}\Gamma - \int_{\partial\Omega_e^{\text{up}}} \lambda(x)a(\{x-\dot{\gamma}Ht\}^{*},0,t)\,\mathrm{d}\Gamma. \tag{37}$$

The Lagrangian multiplier is represented by

$$\lambda = \sum_{i=1}^{M} \lambda_i \psi_i(\xi), \tag{38}$$

in which ψ_i is the spectral element basis function and $M-1$ the order of the approximation. The procedure we follow here in the context of spectral elements is similar to the mortar finite element method [9]. A spectral element method [10,11] is used, since this method is suitable for capturing interfaces with a small interfacial thickness [12]. Similar to a finite element method, the computational domain Ω is divided into N_{el} non-overlapping sub-domains Ω_e, but now a spectral approximation is applied on each element.

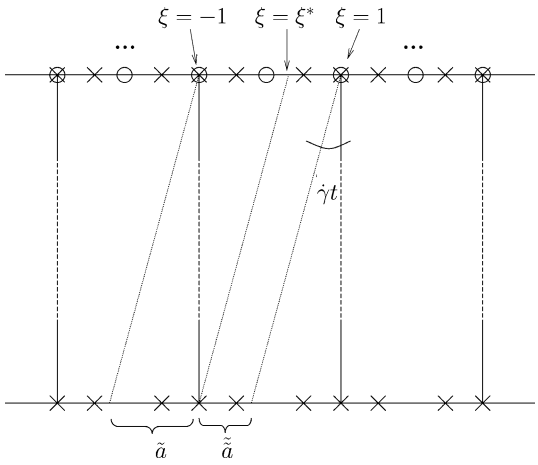

Fig. 3. Example of shifted coupling with third-order spectral elements (×) and second-order Lagrangian multipliers (○).

Essentially, the spectral element basis functions ψ_i are high-order Lagrangian interpolation polynomials through the Legendre–Gauss–Lobatto integration points defined per element. A Legendre–Gauss–Lobatto grid is constructed in each of the elements Ω_k, $1 \leqslant k \leqslant K$, where the grid G_N is a tensor product of one-dimensional Legendre–Gauss–Lobatto grids $G_N = G_{x,N} \otimes G_{y,N}$, where $G_{x,N}$ and $G_{y,N}$ are the ordered sets $\{z_j | j = 0, \cdots, N\}$ of the roots of

$$(1 - z^2)\frac{\mathrm{d}}{\mathrm{d}z}L_n = 0, \tag{39}$$

where L_n is the nth-order Legendre polynomial.

Similarly as for the discretization of the for Lagrangian multiplier, the unknown a is described as:

$$a = \sum_{j=1}^{N} a_j \phi_j(\xi), \tag{40}$$

in which $N - 1$ is again the order of the approximation. Evaluating the first part of the integral in equation (37) gives

$$\int_{\partial\Omega_e^{\mathrm{up}}} \lambda(x) a(x, H, t)\, \mathrm{d}\Gamma = \int_{-1}^{1} \left(\sum_{i=1}^{M} \lambda_i \psi_i(\xi)\right) \cdot \left(\sum_{j=1}^{N} a_j \phi_j(\xi)\right) \left|\frac{\mathrm{d}x}{\mathrm{d}\xi}\right| \mathrm{d}\xi = \left|\frac{\mathrm{d}x}{\mathrm{d}\xi}\right| \sum_{j=1}^{N} \sum_{i=1}^{M} \lambda_i a_j I_{ij}, \tag{41}$$

with

$$I_{ij} = \int_{-1}^{1} \psi_i \phi_j \, \mathrm{d}\xi.$$

The integrals I_{ij} are determined exactly. The analysis of the second part of the integral in Eq. (37) is not as straightforward as the first part. The argument of a, which is shifted with $\dot{\gamma}Ht$ (modulo L), does not necessarily have to coincide with a nodal point on the top boundary, as is illustrated in Fig. 3. The element is therefore divided and integrated separately over the two domains $([-1, \xi^*], [\xi^*, 1])$.

The second integral in Eq. (37) is now split over the two domains:

$$\int_{\partial\Omega_e^{\mathrm{up}}} \lambda(x) a(\{x-\dot{\gamma}Ht\}^*,0,t)\,\mathrm{d}\Gamma = \int_{-1}^{\xi^*}\left(\sum_{i=1}^{M}\lambda_i\psi_i(\xi)\right)\cdot\left(\sum_{j=1}^{N}\tilde{a}_j\phi_j(\xi-\xi^*+1)\right)\left|\frac{\mathrm{d}x}{\mathrm{d}\xi}\right|\mathrm{d}\xi + \int_{\xi^*}^{1}\left(\sum_{i=1}^{M}\lambda_i\psi_i(\xi)\right)\cdot\left(\sum_{j=1}^{N}\tilde{\tilde{a}}_j\phi_j(\xi-\xi^*-1)\right)\left|\frac{\mathrm{d}x}{\mathrm{d}\xi}\right|\mathrm{d}\xi = \left|\frac{\mathrm{d}x}{\mathrm{d}\xi}\right|\left(\sum_{j=1}^{N}\sum_{i=1}^{M}\lambda_i\tilde{a}_j\tilde{K}_{ij}(\xi^*)+\sum_{j=1}^{N}\sum_{i=1}^{M}\lambda_i\tilde{\tilde{a}}_j\tilde{\tilde{K}}_{ij}(\xi^*)\right),$$

with

$$\tilde{K}_{ij}=\int_{-1}^{\xi^*}\psi_i(\xi)\phi_j(\xi-\xi^*+1)\,\mathrm{d}\xi \quad\text{and}\quad \tilde{\tilde{K}}_{ij}=\int_{\xi^*}^{1}\psi_i(\xi)\phi_j(\xi-\xi^*-1)\,\mathrm{d}\xi, \tag{42}$$

where $\tilde{a}$ and $\tilde{\tilde{a}}$ are the unknowns in different elements, as illustrated with the lying brackets in Fig. 3. The coefficients $\tilde{K}_{ij}$ and $\tilde{\tilde{K}}_{ij}$ are again determined exactly.

After the final construction of a linear set of equations, the 'multifrontal method' as used by the MA41 solver from the HSL-library [13] for sparse unsymmetric systems proves to work very well and is used in all simulations including the bi-periodic boundary conditions.

5. Results

The implementation of the streamfunction–vorticity formulation in sliding bi-period frames is validated using a mathematical test problem and the convergence of the model is studied. In Sections 5.2 and 5.3 the model is combined with a diffuse-interface technique so that drop coalescence can be studied in bulk shear flow.

5.1. hp-Convergence

To validate the use of Lagrangian multipliers to couple top and bottom elements a bi-periodic testing function has to be used: $f(x,y)=f(x+L,y)$ and $f(x,y)=f(x,y+H)$, with L the width and H the height of the domain. Second, a new testing function with a shifted argument is defined: $g(x,y)\equiv f(x-\dot{\gamma}yt,y)=f(\hat{x},y)$, introducing $\hat{x}=x-\dot{\gamma}yt$. To validate the model we introduce

$$f(x,y)=\sin(\pi x)\sin(\pi y), \tag{43}$$

to generate the exact solution $u(x,y)=g(x,y)=f(\hat{x},y)$.

Fig. 4 shows the testing function after the first time step (only slightly sheared) and after a full period T, which is the amount of time needed to slide a window completely. A material point at $y=1$ has then moved exactly the entire length of the domain.

For validation purposes the Poisson equation $-\Delta u=h$ is considered where the right-hand side is given by

$$h=-\frac{\partial^2 g}{\partial x^2}-\frac{\partial^2 g}{\partial y^2}=(2+\dot{\gamma}^2t^2)\pi^2\sin(\pi\hat{x})\sin(\pi y)+2\dot{\gamma}t\pi^2\cos(\pi\hat{x})\cos(\pi y). \tag{44}$$

Subsequently, with a known right-hand side, the Poisson equation with a Lagrangian multiplier on the boundary can be solved using spectral approximation with different polynomial orders, and the error can be calculated with respect to the known exact solution. The results of the error, $\|u-u_h\|_\infty$, where u_h denotes the approximate solution, using sixth-order spectral element interpolation functions for u are summarized in Fig. 5.

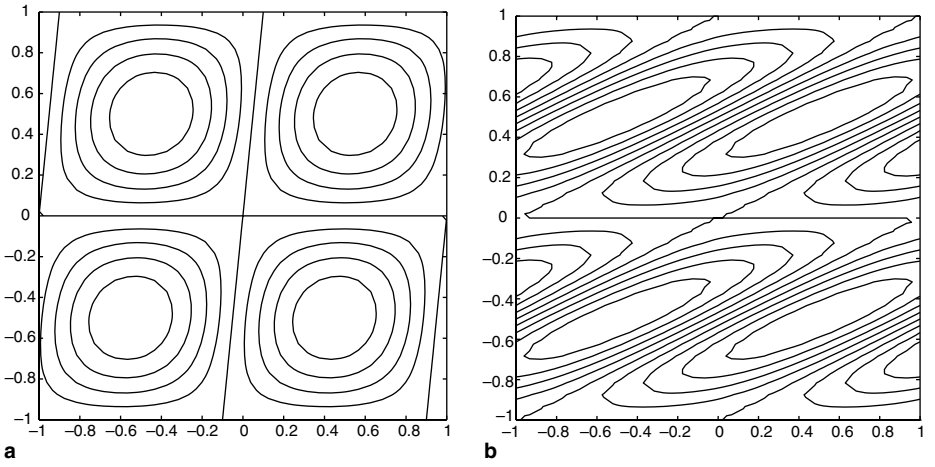

Fig. 4. Testing function $g(x, y)$ after first time step (a) $t = 0.1$, and after a full period (b) $t = 2$.

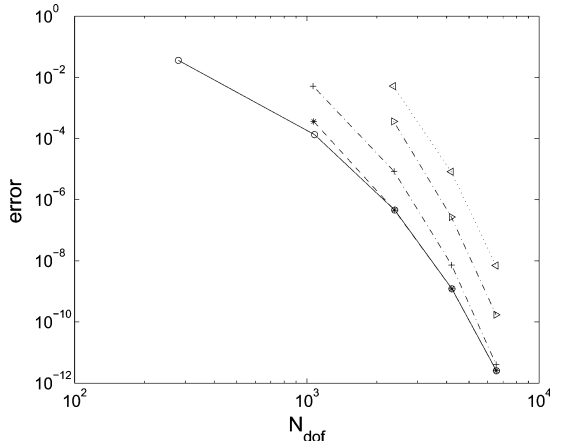

Fig. 5. The error as function of the number of degrees of freedom (N_{dof}). The function is approximated using sixth-order spectral element interpolation functions and the Lagrangian multiplier is approximated with (○) one order, (∗) two orders, (+) three orders, (▷) four orders, (◁) five orders lower in an element.

The trends in Fig. 5 are in line with known theory on *hp* finite element methods [14]. The error $\|u - u_h\|_\infty$ as a function of the number of degrees of freedom shows a more than linear decrease on a log-log scale, indicating spectral convergence. Furthermore, Fig. 5 shows the relation between the error and the difference between the order of the unknown and the Lagrangian multiplier. Seshaiyer and Suri [14] also showed that there is little difference in the error if the order of the Lagrangian multiplier is chosen two orders lower with respect to the spectral order of the unknowns ((∗) broken line), rather than only one order difference ((○) solid line). The error becomes substantially larger if the order difference is higher than two ((+) dash-dot line and triangles (▷◁)). In the remainder of the paper the order of approximation of the Lagrangian multiplier is chosen one order lower.

Fig. 6 shows the *h*-convergence for two different polynomial orders. Increasing the number of elements in the domain yields a linear decreasing error on a log–log scale. This plot shows again the more than linear *p*-convergence, as the slope of higher-order elements decreases faster.

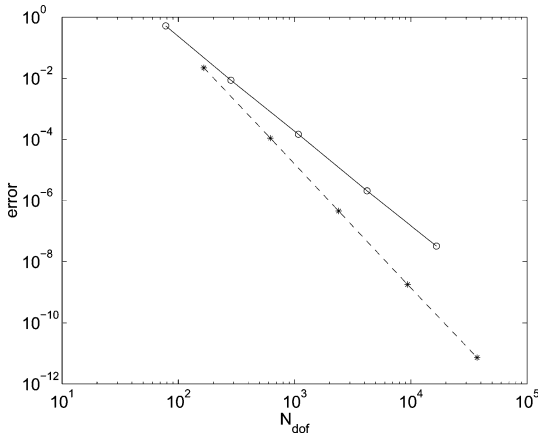

Fig. 6. *h*-Convergence with the error as function of the number of free degrees of freedom, (○) fourth-order spectral elements, (∗) sixth-order elements.

For the testing problem with a Lagrangian multiplier on the top and bottom boundary, an analytical solution can be obtained for the Lagrangian multiplier

$$\lambda = \left.\frac{\partial g}{\partial y}\right|_{y=1} = \left.\left(\frac{\partial f}{\partial y} - \dot{\gamma} t \frac{\partial f}{\partial x}\right)\right|_{y=1} = \left.(\pi \sin(\pi \hat{x}) \cos(\pi y) - \dot{\gamma} t \pi \cos(\pi \hat{x}) \sin(\pi y))\right|_{y=1} = -\pi \sin(\pi \hat{x}). \tag{45}$$

The results are summarized in Fig. 7. The numerically solved values (○, ∗) coincide with the exact solution (solid and broken line), and the corresponding errors are plotted in the bottom and reflect the difference in polynomial order. If the Lagrangian multiplier is of fourth order, the error with the exact solution is of order 10^{-6}, whereas the order of the error is 10^{-3} if only a second-order Lagrangian multiplier is used.

5.2. Drop coalescence

The sheared periodic boundary conditions are used to study drop deformation and coalescence in a bi-period frame. In this section we limit ourselves to two drops and in the following section results are shown with multiple drops where the processes of drop deformation, break up and coalescence occur simultaneously. To model these processes we use the diffuse-interface model which has a long history in fluid mechanics [15–17], especially in the field of phase separation. Recently the method has been applied to study various phenomena that occur in immiscible fluids [18–22].

The classical expression for the Ginzburg–Landau (GL) free energy f_{GL} used in diffuse-interface modeling is based on the work of Cahn and Hilliard [23]

$$f_{\mathrm{GL}}(c, \nabla c) = f_0(c) + \frac{1}{2}\varepsilon |\nabla c|^2 = -\frac{1}{2}\alpha c^2 + \frac{1}{4}\beta c^4 + \frac{1}{2}\varepsilon |\nabla c|^2, \tag{46}$$

where α and β are positive constants and ε is the gradient energy parameter that is proportional to the interaction parameter χ and c is the mass fraction of one of the two components. The chemical potential is obtained from the variational derivative with respect to concentration

$$\mu = \frac{\delta f_{\mathrm{GL}}}{\delta c} = -\alpha c + \beta c^3 - \varepsilon \nabla^2 c.$$

In order to comply with mass conservation for both components, the balance equation should be fulfilled:

$$\frac{\mathrm{d}c}{\mathrm{d}t} = \frac{\partial c}{\partial t} + \nabla \cdot (c\boldsymbol{v}) = \nabla \cdot M \nabla \mu, \tag{47}$$

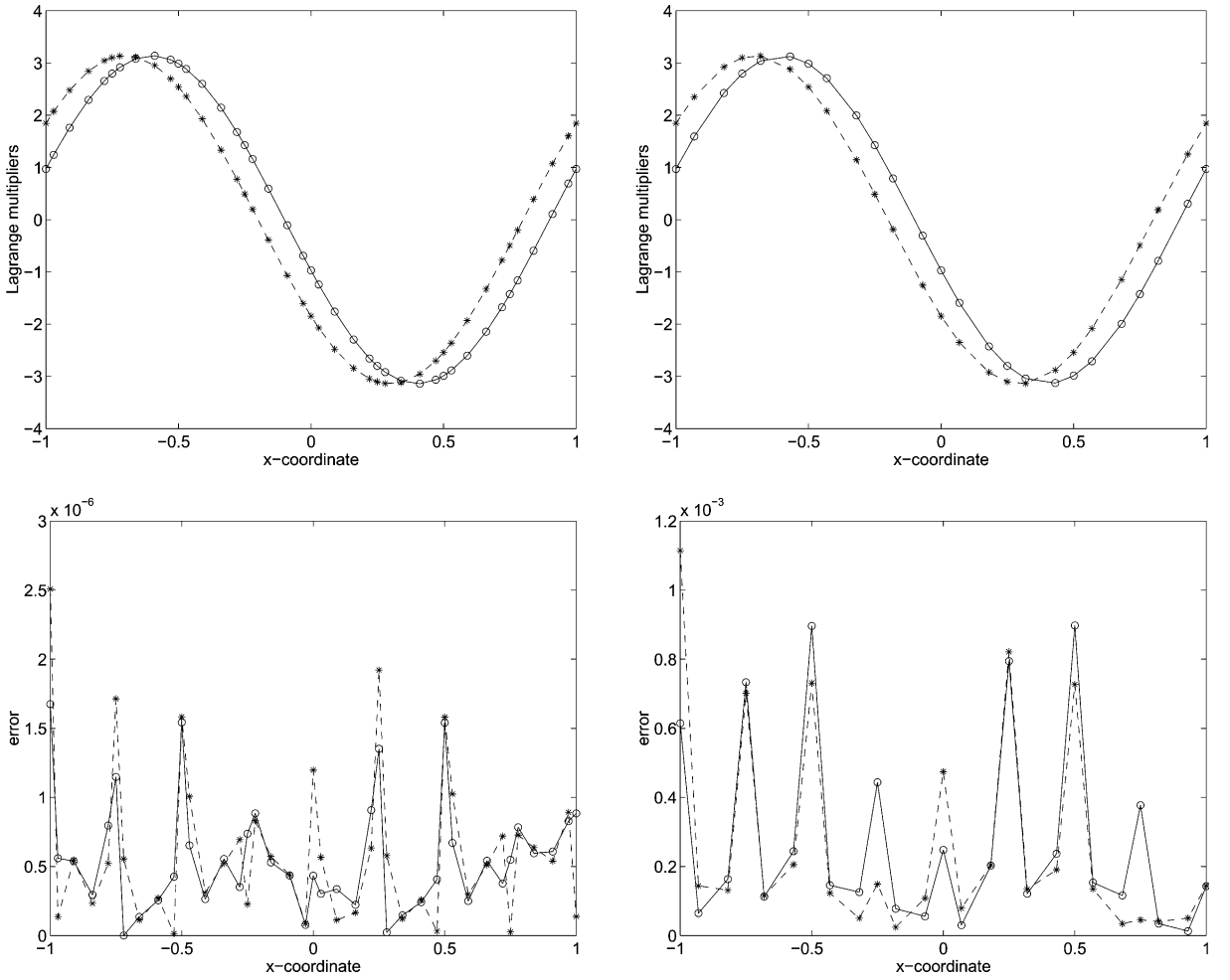

Fig. 7. Numerical results of the Lagrangian multipliers ((○) $t = 0.1$, and (∗) $t = 0.2$) for the testing function $g(x, y)$ together with the exact solution ($t = 0.1$: solid line (—) and $t = 0.2$: broken line (---)) and corresponding errors (bottom), for fifth-order elements (left) and third-order elements (right).

with M the mobility, which is taken constant for simplicity in this work. The diffusion flux is assumed to be proportional to the gradient of the chemical potential, which is more general than the common Fickian diffusion, based on the concentration gradient ∇c, that does not hold for multiphase systems even at equilibrium. We note that to describe a real polymer blend, taking into account long chains and for example block copolymers, the GL free energy is too simple and more complex formulations should be considered. However, the GL free energy will yield a correct qualitative behavior of a polymer blend in shear flow as shown further in Fig. 13. In the following the focus is on the combination of Lees–Edwards boundary condition and the streamfunction–vorticity formulation and more complex thermodynamical descriptions are beyond the scope of this paper.

To obtain momentum conservation, a generalized Navier–Stokes equation can be derived for the velocity field [16]

$$\rho\left[\frac{\partial \boldsymbol{v}}{\partial t} + (\boldsymbol{v}\cdot\nabla)\boldsymbol{v}\right] = -\rho\nabla g_{\mathrm{GL}} + \nabla\cdot\eta(\nabla\boldsymbol{v} + \nabla\boldsymbol{v}^T) + \rho\mu\nabla c. \tag{48}$$

Here g_{GL} is the Gibbs free energy $g_{GL} = f_{GL} + p/\rho$, with p the local pressure and ρ the density. The viscosity η generally depends on c but only here, without any serious restrictions, the iso-viscous case will be considered. Compared to the Navier–Stokes equations, in Eq. (48) only one extra capillary term $\rho\mu\nabla c$ appears which reflects the interfacial tension. This modification accounts for hydrodynamic interactions, i.e. the influence of the concentration c or the morphology on the velocity field and, hence, describes the spatial variations of the velocity field due to the presence of interfaces.

In absence of inertia, the left-hand side of Eq. (48) vanishes and after taken the curl of the remaining equation we get:

$$\eta\nabla^4\psi = \rho\nabla \times \mu\nabla c. \tag{49}$$

In dimensionless form the complete set of equation reads:

$$\frac{\mathrm{d}c}{\mathrm{d}t} = \frac{1}{Pe}\nabla^2\mu, \tag{50}$$

$$\mu = c^3 - c - C^2\nabla^2 c, \tag{51}$$

$$\nabla^4\psi = \frac{1}{Ca}\frac{1}{C}\nabla \times \mu\nabla c, \tag{52}$$

where three dimensionless groups are appearing in the governing equations: the Péclet number Pe, the capillary number Ca and the Cahn number C. For more details see [21]. These equations are solved with Lees–Edwards boundary conditions similar to (ψ, ω).

Two drops are considered coalescing in a shear field, at the same distance and position relative to each other, but at different positions in the domain, see Fig. 10. From a mathematical point of view one expects an identical result, however, since the convective- and diffusive part of the Cahn–Hilliard equation are discretized and numerically solved, different results can be expected depending on the time step. Sixth-order spectral elements are used to approximate the unknowns (ψ, ω, c, μ); for the Lagrangian multiplier again one order lower is chosen.

Fig. 8(a) shows the two drops in the initial shear field, unperturbed by interfacial forces. Fig. 8(b) shows the same two drops after the fifth time step at $t = 0.05$, but now with the velocity due to shear subtracted. The effect of the interfacial forces can be clearly observed.

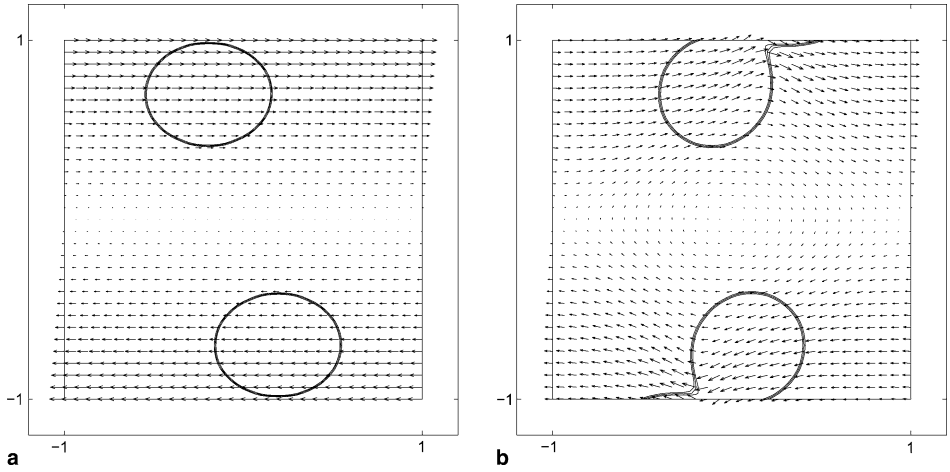

Fig. 8. (a) Combined concentration contour plot and velocity vector plot for two coalescing drops in shear flow (initial field $t = 0$). (b) the velocity due to shear is subtracted. The velocity vectors are due to interfacial forces ($t = 0.05$).

Fig. 9 shows the combined mesh discretization and contour lines for the two coalescing drops. In the high-order spectral element mesh, the non-equidistant Legendre–Gauss–Lobatto integration points can be observed, and the closeup gives an idea of the number of integration points describing the interface.

The simulation as shown in Fig. 10 describes coalescence under weak shearing conditions where $Ca = 0.1$. The first and third row show how two drops coalesce in the center of the domain and how interfacial forces minimize the interfacial area. The second and fourth row show the results of the simulation with the same drops at the same relative initial distance, but at a different position in the domain. The two simulations appear to be similar, based on the assessment of the morphology pictures. Fig. 11 quantifies the small differences between the two simulations showing the maximum vorticity $\max|\nabla^2\psi|$, which is a measure for the coalescence time, with the time step as the varying parameter. A similar criterium was used by Verschueren [24] to test scaling laws in diffuse-interface modeling for coalescing drops.

With decreasing time step convergence of the curves is found, although and a sufficient accuracy is obtained with a time-step of $\Delta t = 10^{-3}$.

5.3. Multi-drop flow

Finally, a multi-drop case is considered where we make a qualitative comparison of the influence of Dirichlet versus Lees–Edwards boundary conditions on the evolving morphology. The results are shown in Fig. 12. The column on the left depicts the results where we used Dirichlet boundary conditions to prescribe the shear flow; the column on the right are with Lees–Edwards boundary conditions. The initial distribution of drops was the same in both cases; 36 drops, with different drop radii, are placed in the domain at $t = 0$. During startup of the shear flow the same deformation behavior is observed in both cases. But after $t = 0.6$ differences appear in the drop morphology close to the moving walls. Even clearer is the influence of the boundary condition at $t = 0.9$ and $t = 1.5$. Here, we observe that in case of Dirichlet boundary

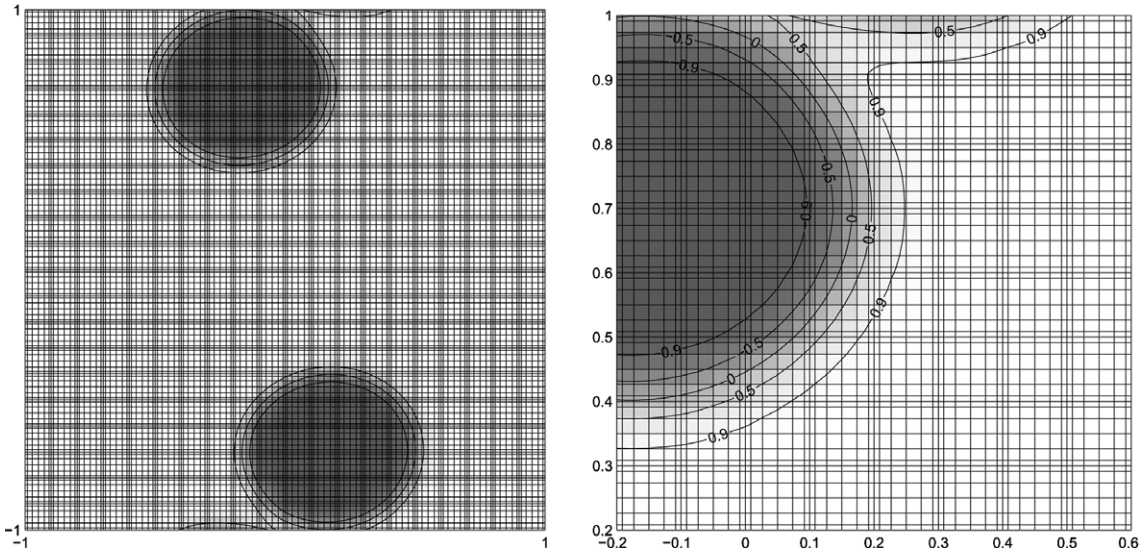

Fig. 9. Sixth-order spectral element mesh ($t = 0.05$) for two coalescing drops and closeup with concentration contour lines $[-0.9\,-0.5\,0\,0.5\,0.9]$.

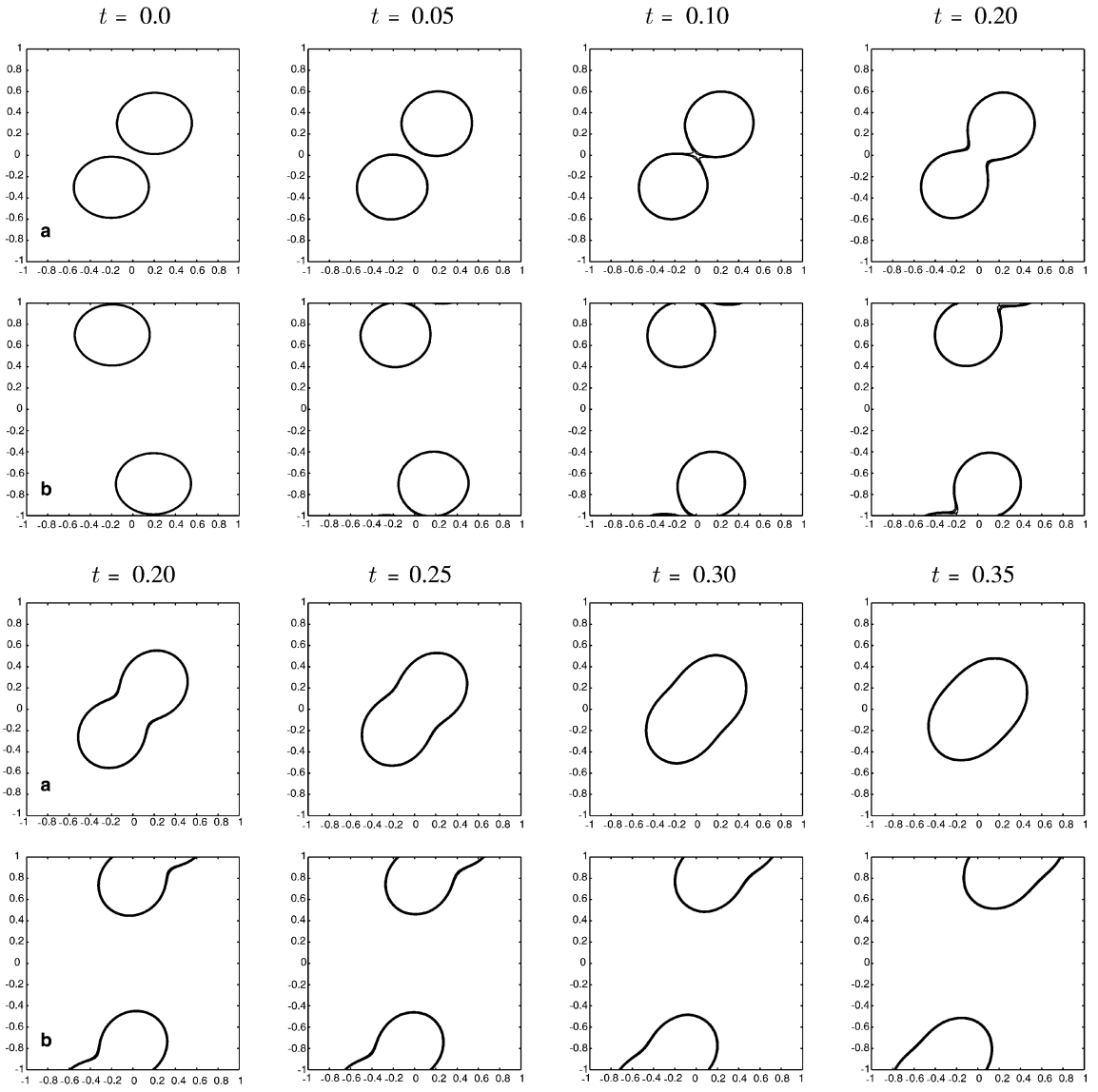

Fig. 10. Concentration contour lines [−0.1 0 0.1] of two coalescing drops at exactly the same distance but at different positions in the domain, calculated with $C = 0.04$, $Pe = 1/C$, $Ca = 0.1$ and $\Delta t = 10^{-2}$. (a) Coalescence in the domain, (b) coalescence over the domain boundary.

conditions, the drops are attached to the wall and have a fixed contact angle of 90°. Deformation and topological transitions are not possible at the moving walls.

In the column on the right we are looking at a bi-period frame so that drops at the bottom wall are 'connected' with drops at the top wall. In this case we do not have a contact angle, which eventually will always influence the bulk behavior, and drop deform across the boundaries. For flow problems like these it is essential that the Lees–Edwards boundary conditions are used in order to get bulk behavior.

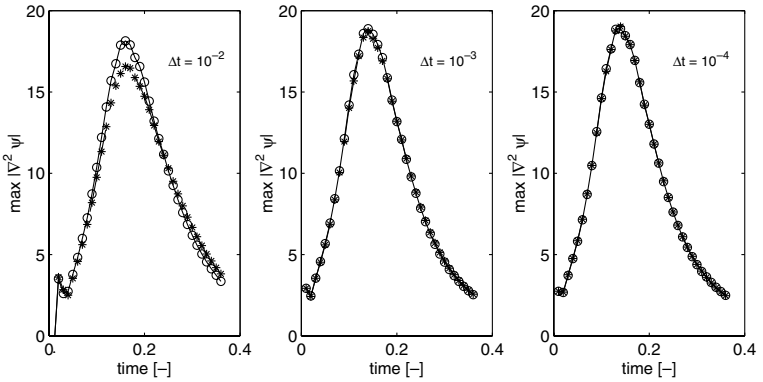

Fig. 11. The maximum vorticity as a function of time for two coalescing drops across the top and bottom boundary ((∗), broken line) and in the center of the domain ((○), solid line), but at the same initial relative distance, simulated with different time steps ($\Delta t = 10^{-2}$, $\Delta t = 10^{-3}$ and $\Delta t = 10^{-4}$) to show time convergence.

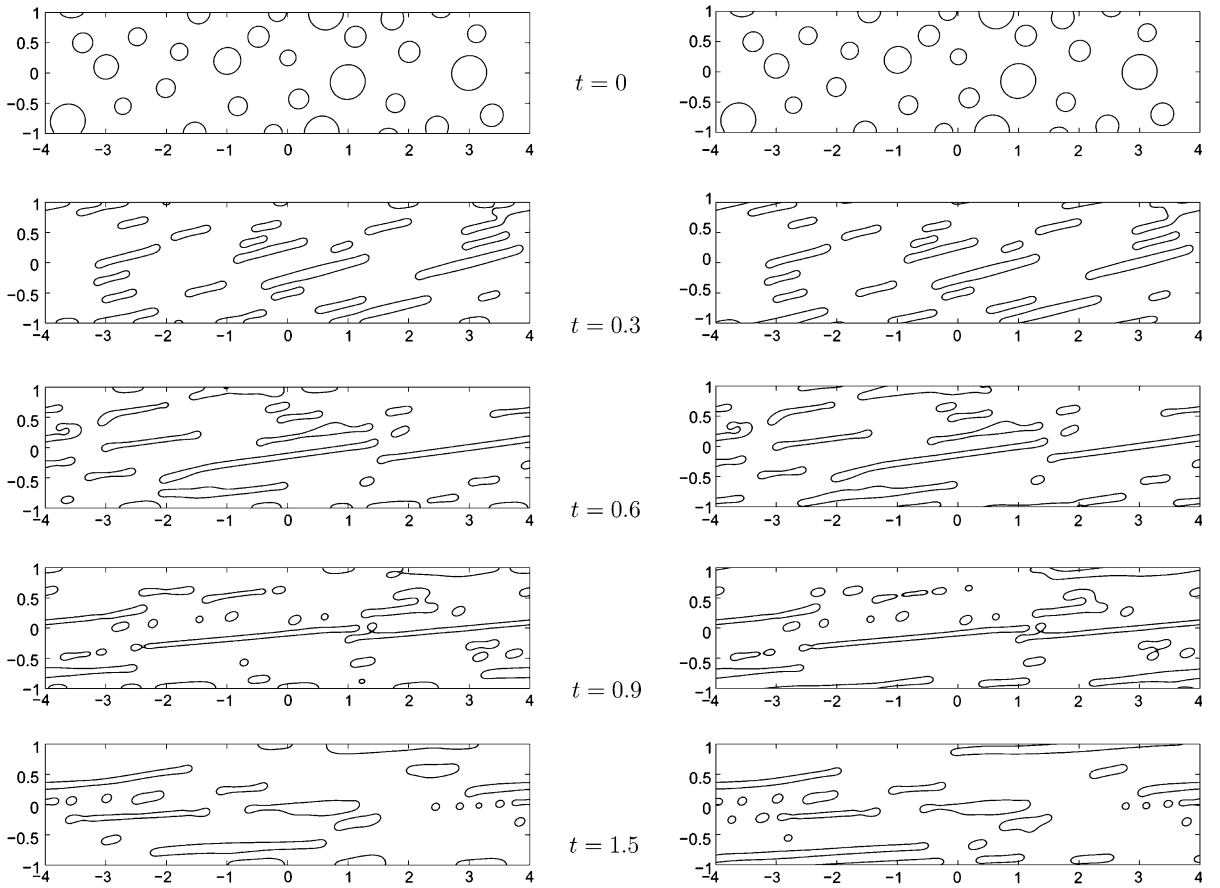

Fig. 12. Multi-drop deformation in shear flow. The column on the left depicts the results where we used Dirichlet boundary conditions to prescribe the shear flow; the results in the column on the right are with the Lees–Edwards boundary conditions.

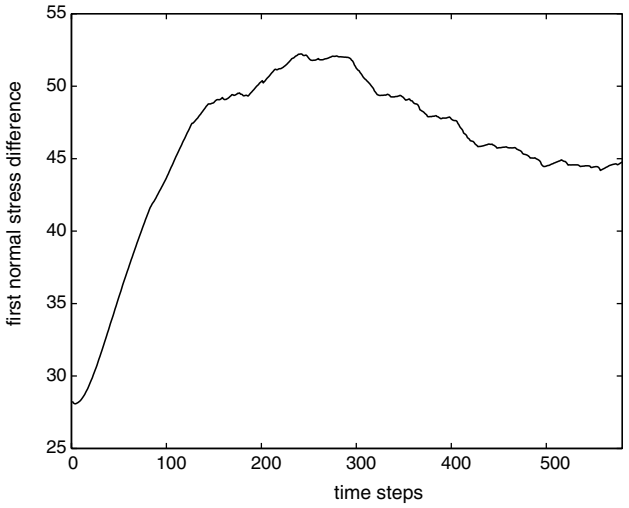

Fig. 13. First-normal stress difference versus time.

The first-normal stress difference has proven to be extremely sensitive to morphological changes in immiscible blends (e.g. [1,25]). To determine the first-normal stress difference N_1 we use the following relation:

$$\frac{N_1}{\Gamma} = q_{yy} - q_{xx}, \tag{53}$$

which can be calculated straightforwardly by using the results of the diffuse interface simulations. Here q_{xx} and q_{yy} are the components of the anisotropy tensor

$$\boldsymbol{q} = \frac{1}{V}\int_S \left(\boldsymbol{nn} - \frac{1}{3}\boldsymbol{I}\right) \mathrm{d}S,$$

where Γ is the interfacial tension, V is the volume of the fluid, S its surface and $\boldsymbol{n}$ denotes the normal at the interface.

Fig. 13 shows the corresponding first-normal stress difference. The evolution of the calculated N_1 is similar to the experimentally observed evolutions of N_1 [26–28]. Initially, during the deformation of the drops, N_1 increases. When the drops breakup, the anisotropy of the structure decreases and consequently the first-normal stress difference is reduced. Finally, a steady state deformation and hence constant N_1 is reached. The noise in the curve in Fig. 13 is due to the fact that only a relatively small number of drops is used in the calculations. Increasing their number will reduce the statistical noise and smooth the curve.

6. Conclusions

The Lees–Edwards description of bi-periodic boundary conditions has been extended to the streamfunction and streamfunction–vorticity formulation in sliding bi-periodic frames. The required compatibility conditions are formulated and uniqueness of the solution in both formulations is shown. Lagrangian multipliers are used to introduce coupling in the shifted periodic fashion. A spectral element discretization is applied to solve the flow equations. From the validation results of this method it can be concluded that, if the order of the Lagrangian multipliers is chosen two orders lower than the order of the

unknowns, no significant loss of accuracy is observed with respect to the results with only one order difference between the unknowns and Lagrangian multipliers. This is in line with the recently appeared literature [14].

In addition in this paper it is shown that the boundary conditions can have a large influence on the morphology that develops and that they require special attention if bulk behavior is subject of study. Bi-periodic boundary conditions can be used to eliminate unwanted wall effects but make it impossible to apply shear on the system. In order to describe bulk shear behavior one needs to use the concept of a sliding periodic frame.

Acknowledgments

The authors acknowledge the contribution of Dr. W.R. Hwang by providing his notes on implementing Lees–Edwards boundary conditions.

Appendix A. Uniqueness of streamfunction ψ and vorticity ω

The uniqueness of ω can be tested as follows. Assume that there are two solutions ω_1 and ω_2 fulfilling Eq. (34). Then we find by subtracting the equations that

$$(\nabla(\omega_1 - \omega_2), \nabla w_1) = 0, \tag{A.1}$$

for all continuous sheared periodic test functions w_1. Now take $w_1 = \omega_1 - \omega_2$ and we find that

$$\int_\Omega |\nabla(\omega_1 - \omega_2)|^2 \, \mathrm{d}\Omega = 0, \tag{A.2}$$

leading to

$$\nabla(\omega_1 - \omega_2) = 0 \quad \text{or} \quad \omega_1 = \omega_2 + c, \tag{A.3}$$

where c is an arbitrary constant. This shows that ω can be determined up to an arbitrary constant from Eq. (34), which is a general result for a Poisson equation in a sheared periodic region. As has been shown in the previous section, the integration constant for ω can be determined from the compatibility condition (26) and therefore ω is unique.

With the same reasoning and given ω it is easy to show that from Eq. (35) we can uniquely determine ψ up to an integration constant. This constant is of no significance for the flow and can be specified by giving ψ an arbitrary value at a some point in the flow.

We have now shown that the streamfunction–vorticity formulation leads to a unique solution (up to an integration constant for ψ). We still have to show that this solution for ψ is identical to the one found within a streamfunction formulation. In essence it means that we have to show that the boundary conditions are the same or consistent, because the equations inside the domain are identical (Eq. (11) follows directly from Eqs. (22) and (23)). We follow again the route of the weak form. After multiplying Eq. (11) with a test function w, integrating over the domain and partial integrating twice, we find that

$$(\nabla^2\psi, \nabla^2 w) + \left(\frac{\partial}{\partial n}(\nabla^2\psi), w\right)_\Gamma - \left(\nabla^2\psi, \frac{\partial w}{\partial n}\right)_\Gamma = (g, w) \quad \text{for all } w. \tag{A.4}$$

Now we assume that the test function w is continuous sheared periodic with further requirement that $\partial w/\partial n$ fulfills

$$\begin{aligned}\frac{\partial w}{\partial n}(0,y,t) &= -\frac{\partial w}{\partial n}(L,y,t) \quad \text{for } y \in [0,H],\\ \frac{\partial w}{\partial n}(x,H,t) &= -\frac{\partial w}{\partial n}(\{x-\dot{\gamma}Ht\}^{\star},0,t) \quad \text{for } x \in [0,L).\end{aligned} \tag{A.5}$$

Furthermore, we assume that ψ is continuous sheared periodic and $\partial\psi/\partial n$ obeys Eq. (33). We also assume that $\nabla^2\psi$ is continuous sheared periodic and $\partial(\nabla^2\psi)/\partial n$ fulfills

$$\begin{aligned}\frac{\partial(\nabla^2\psi)}{\partial n}(0,y,t) &= -\frac{\partial(\nabla^2\psi)}{\partial n}(L,y,t) \quad \text{for } y \in [0,H],\\ \frac{\partial(\nabla^2\psi)}{\partial n}(x,H,t) &= -\frac{\partial(\nabla^2\psi)}{\partial n}(\{x-\dot{\gamma}Ht\}^{\star},0,t) \quad \text{for } x \in [0,L).\end{aligned} \tag{A.6}$$

Using the assumptions given above we can now derive the weak form from Eq. (A.4): Find the continuous sheared periodic ψ, fulfilling Eq. (33) for $\partial\psi/\partial n$ such that

$$(\nabla^2\psi, \nabla^2 w) = (g, w), \tag{A.7}$$

for all continuous sheared periodic functions w, fulfilling Eq. (A.5) for $\partial w/\partial n$. Reversely, when the weak form is satisfied we can easily derive the original biharmonic equation (11), the continuous sheared periodicity of $\nabla^2\psi$ and Eq. (A.6) for $\partial(\nabla^2\psi)/\partial n$. Note, that within a variational context both ψ and $\partial\psi/\partial n$ are primary variables ('displacements'), whereas $\nabla^2\psi$ and $\partial(\nabla^2\psi)/\partial n$ are natural variables ('tractions'). Using $\omega = -\nabla^2\psi$ we see that the boundary conditions used in the streamfunction formulation are the same as in the streamfunction–vorticity formulation, which shows the equivalence of the two formulations. This is quite different for the more common case that Dirichlet conditions for ψ and $\partial\psi/\partial n$ are specified on the boundary. In that case, complicated integral type boundary conditions for ω need to be specified in order to obtain an equivalent formulation [8].

The compatibility equation (20) is found from the weak form Eq. (A.7) by taking $w = 1$. Note, that taking $w = x$ or $w = y$ is not allowed, because these functions are not continuous sheared periodic.

The uniqueness of ψ can be found by assuming two solutions ψ_1 and ψ_2 fulfilling both the weak form Eq. (A.7). By subtracting these equations we get

$$(\nabla^2(\psi_1 - \psi_2), \nabla^2 w) = 0, \tag{A.8}$$

for all continuous sheared periodic functions w, fulfilling Eq. (A.5) for $\partial w/\partial n$. If we take $w = \psi_1 - \psi_2$, which is allowed, we find that

$$\nabla^2(\psi_1 - \psi_2) = 0 \text{ in } \Omega. \tag{A.9}$$

Similar to the vorticity equation we can determine $\psi_1 - \psi_2$ up to an integration constant from this equation. This result is consistent with the result from the streamfunction–vorticity formulation, as it should, since we already showed both formulations are equivalent.

References

[1] C.L. Tucker, P. Moldenaers, Microstructural evolution in polymer blends, Ann. Rev. Fluid Mech. 34 (2002) 177–210.
[2] A.W. Lees, S.F. Edwards, The computer study of transport properties under extreme conditions, J. Phys. C: Solid State Phys. 5 (1972) 1921.
[3] A.J. Wagner, I. Pagonabarraga, Lees Edwards boundary conditions for lattice Boltzmann, J. Stat. Phys. 107 (2002) 521.
[4] A.J. Wagner, J.M. Yeomans, Phase separation under shear in two-dimensional binary fluids, Phys. Rev. E 59 (1999) 4366–4373.
[5] A. Lamura, G. Gonnella, Lattice Boltzmann simulations of segregating binary fluid mixtures in shear flow, Physica A 2001 (2001) 295.
[6] M. Doi, X.F. Yuan, A general approach for modelling complex fluids: its application to concentrated emulsions under shear, Colloids Surf. A 144 (1998) 305.

[7] W.R. Hwang, M.A. Hulsen, H.E.H. Meijer, Direct simulation of particle suspensions in sliding bi-periodic frames, J. Comput. Phys. 194 (2004) 742–772.
[8] L. Quartapelle, F. Valz-Gris, Projection conditions on the vorticity in viscous incompressible flows, Int. J. Numer. Meth. Fluids 1 (1981) 129–144.
[9] F.B. Belgacem, The mortar finite element method with Lagrangian multipliers, Numer. Math. 84 (1999) 173–197.
[10] A.T. Patera, A spectral element method for fluid dynamics, J. Comput. Phys. 54 (1984) 468–488.
[11] L.J.P. Timmermans, F.N. van de Vosse, P.D. Minev, Taylor–Galerkin-based spectral element methods for convection–diffusion problems, Int. J. Numer. Meth. Fluids 18 (1994) 853–870.
[12] M. Verschueren, P.D. Anderson, F.N. van de Vosse, A high order interface capturing technique for structure development in binary fluids, in: ICOSAHOM'98, J. Non-Newton. Fluid June 22–26, Herzliya, Israel, 1998.
[13] HSL, A collection of Fortran codes for large scale scientific computation, 2002. Available from: <http://www.cse.clrc.ac.uk/nag/hsl/>.
[14] P. Seshaiyer, M. Suri, *hp* Submeshing via non-conforming finite element methods, Comput. Methods Appl. Mech. Eng. 189 (2000) 1011–1030.
[15] D.M. Anderson, G.B. McFadden, A.A. Wheeler, Diffuse-interface methods in fluid mechanics, Annu. Rev. Fluid Mech. 30 (1998) 139–165.
[16] J. Lowengrub, J. Goodman, H. Lee, E.K. Longmire, M.J. Shelley, L. Truskinovsky, Topological transitions in liquid/liquid interfaces, in: I. Athanasopoulos, M. Makrakis, J.F. Rodrigues (Eds.), Proceedings of the 1997 International Congress on Free Boundary Problems, Pitman Research Notes, Addison-Wesley Longman, 1998.
[17] E.B. Naumann, D.Q. He, Nonlinear diffusion and phase separation, Chem. Eng. Sci. 56 (2001) 1999–2018.
[18] R. Chella, J. Viñals, Mixing of a two-phase fluid by cavity flow, Phys. Rev. E 53 (4) (1996) 3832–3840.
[19] D. Jacqmin, An energy approach to the continuum surface tension method, in: Proc. 34th Aerosp. Sci. Meet. Exh., Am. Inst. Aeron. Astron., AIAA 96-0858, Reno, 1996.
[20] T. Roths, C. Friedrich, M. Marth, J. Honerkamp, Dynamics and rheology of the morphology of immiscible polymer blends – on modeling and simulation, Rheol. Acta 41 (2002) 211–222.
[21] B.J. Keestra, P.C.J. Van Puyvelde, P.D. Anderson, H.E.H. Meijer, Diffuse interface modeling of the morphology and rheology of immiscible polymer blends, Phys. Fluids 15 (9) (2003) 2567–2575.
[22] C. Liu, P. Yue, J.J. Feng, J. Shen, A diffuse-interface method for simulating two-phase flows of complex fluids, J. Fluid Mech. 515 (2004) 293–317.
[23] J.W. Cahn, J.E. Hilliard, Free energy of a nonuniform system. I. Interfacial energy, J. Chem. Phys. 28 (2) (1958) 258–267.
[24] M. Verschueren, A diffuse-interface model for structure development in flow. PhD thesis, Eindhoven University of Technology, the Netherlands, 1999.
[25] E.J. Windhab, M. Dressler, K. Feigl, P. Fischer, D. Megias-Alguacil, Emulsion processing – from single drop deformation to design of complex processes and products, Chem. Eng. Sci. 60 (2005) 2101–2113.
[26] I. Vinckier, Microstructural analysis and rheology of immiscible polymer blends, PhD thesis, Katholieke Universiteit Leuven, Belgium, 1996.
[27] T. Jansseune, J. Mewis, P. Moldenaers, M. Minale, P.L. Maffettone, Rheology and rheological morphology determination in immiscible two-phase polymer model blends, J. Non-Newton Fluid Mech. 93 (2000) 153–165.
[28] Y. Takahashi, N. Kurashima, I. Noda, M. Doi, Experimental tests of the scaling relation for textured materials in mixtures of two immiscible fluids, J. Rheol. 38 (1994) 699–712.